Chapter 4

Engineering Magnetoresistance in Mn_xGe_{1-x} System for Magnetic Sensor Application

Tianxiao Nie, Weisheng Zhao and Kang L. Wang

Additional information is available at the end of the chapter

http://dx.doi.org/10.5772/intechopen.70206

Abstract

In 2007, a Nobel Prize is awarded to Dr. Albert Fert and Peter Grünberg for their contribution in giant magnetoresistance (GMR) effect. The magnetic head based on GMR effect has significantly increased the storage density in the hard disk drive (HDD) and brought the coming of the digital age. Besides, the rapid development of GMR sensor has opened a wide and promising range of applications, including the aspects in automobile, traffic monitor, biomedicine, and space, etc. As continuously extending the market, it needs GMR sensor with much lower cost, smaller size, higher sensitivity, and compatibility with the CMOS technology. In light of that, we give a review about the recent progress of the MR effect in Mn_xGe_{1-x} system, which refers to the material growth and magnetic and MR property. Through engineering the Mn_xGe_{1-x} structure, it could realize the transition from negative to positive MR, geometric-enhanced giant MR, and electric-field controlled MR. The fact of well-designed MR effect and high compatibility with Si technology brings a high potential and advantage for fabricating Mn_xGe_{1-x}-based MR sensors, which could be widely used in magnetic head and biomedical sensors, among others, with the superiority of much lower manufacturing cost, lower power dissipation, higher integration density, and higher sensitivity.

Keywords: magnetoresistance, geometric-enhanced MR, electric-field controlled MR, Mn_xGe_{1-x} system, MR sensor

1. Introduction

Magnetic sensors have been widely used in analyzing and controlling thousands of functions by human beings for many decades [1–3]. A digital world has arrived and been driven by the tremendous increase of storage density in the hard disk drive (HDD) using the state-of-the-art

magnetic sensor [4]. The convenient transportation has been promised in a safe manner because of the high reliability of the noncontact switching and monitor with magnetic sensor [5–7]. The portable medical system relies on the magnetic sensor for nondestructive diagnostic applications [8–10]. Factories have high productivity due to the high stability and precision as well as low cost of magnetic sensors [3, 11].

There are numerous types of magnetic sensors [6], such as search-coil sensors, fluxgate sensors, magneto-optical sensors, optically pumped magnetometer, magnetoresistance (MR) sensors, Hall effect sensors, and superconducting quantum interference device (SQUID) magnetometer, among others. Most of them are based on the direct magnetic and electric response. A magnetic sensor can directly convert the magnetic signal into an inductive voltage signal [12] or resistance variation [5], and its sensitivity determines its operating regime and potential applications. For example, SQUID magnetometer with a high sensitivity of 10^{-10}–10^{-4} gauss has been used for measuring magnetic field gradients or differences due to permanent dipole magnets in major applications of brain function mapping. The fluxgate and MR sensor can provide the medium field sensitivity of 10^{-6}–10^{2} gauss, which has been used for the magnetic compass and magnetic anomaly detection. Hall effect sensors with a low sensitivity of 1–10^{6} gauss have been exploited for applications in noncontact switching and current meters. In consideration of the operating regime, the MR sensor is one of the most commonly used sensors in everyday life [4, 5, 11, 13, 14]. Additionally, it demonstrates some specific advantages [4, 5] comparing to others, including high compatibility with the CMOS process technology, high scalability, low power dissipation, and low manufacture cost.

MR sensors using the resistance as the detectable signal involve the contributions from different mechanisms, such as anisotropic magnetoresistance (AMR) [5], giant magnetoresistance (GMR) [5, 15, 16], and tunnel magnetoresistance (TMR) [17, 18]. AMR sensor could exhibit large field sensitivity and more significantly could detect the field direction, which has been widely used as the magnetic head in HDD and automotive sensors to determine many quantities, like throttle valve position, chassis height, and pedal position [5]. However, since the discovery of GMR effect in 1988 [15], it has gradually replaced the role of the AMR effect for the sensor application, which provided more advantages, such as larger output signal, miniaturization opportunity, and the possibility to make a 360° angle sensor. As a derivative of GMR effect, TMR effect could have much higher sensitivity and integration density [18]. A successful paradigm for sensor evolution is the magnetic read head. A dramatic shift to storing data from the analog to current digital world started in the 2000s and was dominantly driven by the emergence of spintronics exemplified by the introduction of the AMR read head in 1991 by IBM [19], the GMR read head in 1997 [20, 21], and the TMR read head in 2006 [21]. Prior to the introduction of the MR read head, the storage densities of HDD had increased at a growth rate of 25% per year. With the introductions of the AMR head in 1991, the growth rate of storage density increased to 60% per year, while the introduction of GMR read head made the growth rate further to 100% per year. Due to such dramatic impact, the 2007 Nobel Prize in Physics was awarded to Albert Fert and Peter Grünberg for the discovery of GMR effect. The recent areal density growth has slowed resulting mainly from the thermal instabilities, known as the superparamagnetic effect [22, 23]. While the continual effort attempts to address the fundamental limitation of GMR sensor for much higher sensitivity and thermal instability, searching for other high-efficient MR sensors has never been stopped.

As a potential candidate, the geometric-enhanced MR could demonstrate a large MR value as a function of magnetic field, and the underlying mechanism arises from the dependence of the current path on the sample shape and electrode configuration [24]. GMR effect can give rise to a negative MR, whereas the geometric-enhanced MR usually is positive. The current deflected from the electric-field direction by Lorentz force, and the inhomogeneity in current path determined the MR sensitivity. Previously, Thio et al. reported a large MR up to 28% at 500 gauss in the inhomogeneous $Hg_{1-x}Cd_xTe$ thin film associated with the composition fluctuation [24, 25]. Furthermore, Solin et al. configured an inhomogeneous structure by embedding concentric gold in nonmagnetic indium antimonide matrix and showed a MR value as high as 100% at 500 gauss [24]. All of these results point to a new way for designing new type of MR sensors, and the related research is still in progress.

As the demand for the sensors with higher integration density and lower manufacturing cost is continuously growing, it calls for not only innovative sensor configuration but also novel material candidate with much higher sensitivity to magnetic field, higher compatibility with CMOS technology, and lower power consumption. Mn_xGe_{1-x} [26] as the silicon-compatible material appears to be an appealing candidate for application in MR sensors through the combined use of GMR [27] and geometric-enhanced MR [28]. In light of that, we give a review of the current research progress in Mn_xGe_{1-x} thin film and nanostructures, as well as their possible application in MR sensors. The fundamental aspects of the MR mechanisms are listed in the first section. The following section gives a systematic and comprehensive review about the Mn_xGe_{1-x} material growth, structure characterization, and MR measurement. MR phenomena based on different mechanisms including GMR, geometric-enhanced MR, and even electric-field controlled MR have been well discussed, and the correlation between the structures and MR properties is established. The final section gives an outlook of the potential application of the Mn_xGe_{1-x}-based MR sensors and estimates their implicit impact. Exploiting Mn_xGe_{1-x}-based MR sensors may set a new stage for the next-generation sensors with improved sensitivity, higher scalability, and higher compatibility with current CMOS technology.

2. The fundamental principles in MR sensors

2.1. The definition of MR effect

The definition of the MR comes from the resistance variation of a material as a function of magnetic field, which can be described by the following equation:

$$MR = \frac{R(B) - R(0)}{R(0)} = f(B) \tag{1}$$

where the R(B) and R(0) are the resistance at the magnetic field of B and zero, respectively. The MR value follows different functions with the magnetic field based on the mechanism differences. In a traditional semiconductor, the MR abides by the orbital MR effect with the origin from Lorentz force. The deflection of the current due to the magnetic field produces an increase of the current path length and thus an increase of resistance. The relation between them can be described as:

$$MR = \frac{\rho_B}{\rho_0}\left(1 + C_1 (\mu B)^2\right) \tag{2}$$

where ρ_B/ρ_0 is the specific relative resistance, C_1 is a geometrical parameter, and μ is the carrier mobility. However, the MR response in such principle is very weak and thus limiting their broad application.

2.2. AMR effect

The AMR effect was initially discovered in 1857 by William Thomson [5]. It happened in the ferromagnetic materials, which arose from the spin-orbit interaction and the resistance depended on the orientation of the current relative to magnetization direction [29]. Usually, the resistance is higher for the current direction parallel to the magnetization and lower for the current perpendicular to the current. Such angle dependence could be described by the following equation:

$$R = R_0 + \Delta R \cos^2 \theta \tag{3}$$

Apparently, the signal extrema are achieved at angles of 0° and 90°, and the steepest response slope is at an angle of 45°. Thus, to achieve the highest sensitivity, the sensor was normally designed with the initial magnetization direction to the current direction at an angle of 45°. Typical AMR response is about 1–4% [5, 29], which is good enough for allowing the use of AMR sensors in practical application.

2.3. GMR effect

GMR was discovered independently by Albert Fert and Peter Grünberg in 1988 [15, 16]. Since then, great progress in improving the GMR value has been achieved, and the use of GMR effect in practical applications has significantly changed the world. The most important application is the use of GMR read head, which has dramatically increased the areal density in HDD and brought the advent of the digital world. The significance of the GMR discovery was recognized by the Nobel Prize in Physics awarded to Fert and Grünberg in 2007. In the GMR effect, the resistance relies on the angle between magnetization directions at different locations in the materials, which could happen in granular systems [30–32] or ferro-/non-ferro-multilayer materials [33, 34]. For real application, the multilayer structure is mainly considered rather than the granular system which is normally in an uncontrollable growth condition. The basic principle of GMR effect is the spin-dependent scattering, in which a parallel direction between the current spin and magnetization can generate a low scattering, while its antiparallel direction is in a high scattering. The resistance as a function of the angle between magnetization directions is described by:

$$R(\theta) = R(0) + \Delta R[1 - \cos\theta]/2 \tag{4}$$

where ΔR is the value of R(180°)–R(0°). This equation can show that the angle dependence of the GMR effect has a period of 360°, which forms an obvious contrast to the AMR effect with a period of 180°.

2.4. TMR effect

As one specific case of GMR, the TMR [35–37] happened as the nonmagnetic conductive layer was substituted by an insulating layer in the multilayer structure, named as magnetic tunnel junction (MTJ). In this structure, electrons can pass through this insulator by means of the quantum tunnel effect. In early reports, the insulating layer in MTJ was constituted by Al_2O_3, which demonstrated a MR level of MTJ about 40% [36]. Recently, this level has been significantly improved to 200% by using MgO as the insulating layer [17, 18]. The improvement of TMR level has significantly increased the areal density of HDD; meanwhile, it has boosted the development of spin-transfer torque-based magnetoresistive random access memory (STT-MRAM) for the next-generation memory application [38].

2.5. Geometric-enhanced MR effect

Geometric-enhanced MR is another specific case of the orbital MR associated with the material shape [24, 28]. A typical structure is consisted of a composite including conductive metal and less conductive semiconductor. The electric field, **E**, is normal to the equipotential surface of the highly conductive metal. The current density is written as $\mathbf{J} = \boldsymbol{\sigma}(H)\mathbf{E}$, where $\boldsymbol{\sigma}(H)$ is the conductivity tensor. At $H = 0$, the tensor of $\boldsymbol{\sigma}(H)$ is diagonal, so $\mathbf{J} = \sigma\mathbf{E}$ and the current flows into the conductive metal, which acts as a short circuit. At high H, the off-diagonal component of $\boldsymbol{\sigma}(H)$ gives rise to a deflection of **J** from **E**, and the deflection angle is called as Hall angle [39], which is dependent on the Hall mobility μ and H. In a sufficiently large H, the current may deflect around the conductive metal and flow in the less conductive semiconductor, which acts as an open circuit. The transition from short circuit at low H to open circuit at high H results in a geometric enhancement of the MR.

3. The research progress of MR effect in Mn_xGe_{1-x} system

3.1. MR effect in the Mn_xGe_{1-x} thin film

Mn_xGe_{1-x} could go through different MR effects through engineering Mn-doping concentration, Mn_xGe_{1-x} phase, and geometric structure. At the beginning, we pay our attention to the MR effect that happens in Mn_xGe_{1-x} thin film. The Mn_xGe_{1-x} thin film was grown on Ge substrate by a Perkin-Elmer solid-source molecular beam epitaxy (MBE) with Ge and Mn Knudsen cells. Ge substrate was cleaned by immersing in acetone and isopropyl alcohol with ultrasonic agitation, followed by dipping in 1% hydrofluoric (HF) acid. Then, the substrate was directly transferred into the MBE chamber for thin-film growth at around 200°C. After growth, its microstructure and composition were comprehensively characterized by transmission electron microscopy (TEM) equipped with energy-dispersive spectroscopy (EDS). Its magnetic property and magnetoresistance were revealed by SQUID and physical property measurement system (PPMS).

Figure 1(a) is a typical cross-sectional TEM image of the grown thin film, which shows some dark parts embedded in the Ge matrix. To understand the detailed structure, high-resolution TEM (HRTEM) was employed, and typical [110] zone axis TEM results are shown in **Figure 1(b)–(d)**.

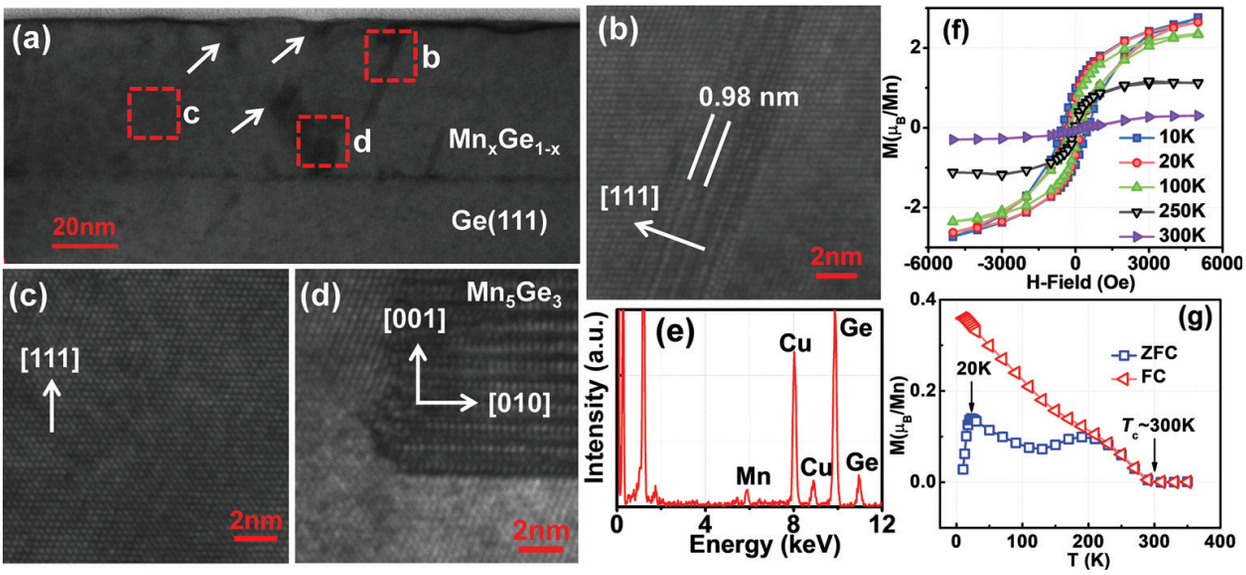

Figure 1. (a) A typical cross-sectional TEM image of the Mn_xGe_{1-x} thin film. (b)–(d) HRTEM images of the stacking faults, Mn_xGe_{1-x} DMS region, and Mn_5Ge_3 cluster in the film, respectively. (e) EDS spectrum confirming the ~4% Mn doping. (f) Temperature-dependent hysteresis loop of the Mn_xGe_{1-x} thin film. (g) ZFC and FC curves, showing a T_c around 300 K. Reproduced with permission from [26]. Copyright 2015, Elsevier.

In **Figure 1(b)**, stacking faults (SFs) could be clearly observed in the Ge matrix and feature a triplet periodicity of Ge (111) lattice spacing [40]. The formation of SFs might come from the strain accumulation of Mn doping and lattice-mismatched precipitates. **Figure 1(c)** was collected from the relatively-uniform doped region and clearly displays a very good crystallinity. Meanwhile, some precipitates could be noticeably observed in the thin-film sample, as shown in **Figure 1(d)**. It clearly shows another set of lattice structure that is different from the Ge matrix. Using the lattice spacing of the Ge as the reference, we calculated the observed lattice spaces of the cluster, which matched well with the (002) and (010) atomic planes of the hexagonal Mn_5Ge_3 phase [41, 42]. Furthermore, it can be confirmed that the Mn_5Ge_3 (002) plane was parallel to the Ge (111) plane. To determine the Mn-doping concentration, EDS was carried out, and the result reveals that the average Mn concentration is ~4%, as shown in **Figure 1(e)**. The magnetic property of the grown Mn_xGe_{1-x} film was measured by SQUID, and the result is shown in **Figure 1(f)**. Magnetic hysteresis can be observed between 10 and 250 K, and it disappears around 300 K. To further determine the T_c and detect any magnetic precipitates, zero-field-cooled (ZFC) and field-cooled (FC) magnetic measurements were performed under a small magnetic field of 200 Oe. As shown in **Figure 1(g)**, the magnetization vanishes near 300 K, indicating a T_c ~ 300 K, which further confirms the formation of Mn_5Ge_3 (T_c ~ 296 K) [43]. Two blocking temperatures coexist in the ZFC curve, with the lower one at 20 K and the higher one at 200 K, which are attributed to Mn-rich coherent Mn_xGe_{1-x} nanostructures [44] and Mn_5Ge_3 precipitates [27], respectively. Both of them could be well resolved in the TEM characterization in **Figure 1(a)**, as indicated by white arrows and red-dotted squares, respectively.

For sensor application, it should explore the MR effect of the Mn_xGe_{1-x} thin film to reveal its control parameters. To this end, the current sample accompanied by a more Mn-doped sample (6%) was fabricated into micrometer Hall bar structures by photolithography for the

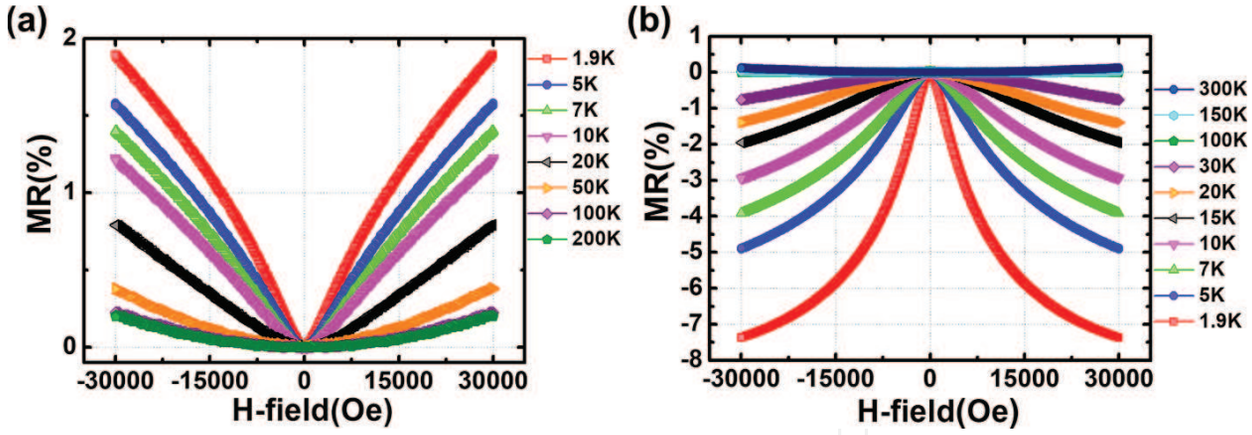

Figure 2. (a)–(b) Temperature-dependent MR of thin films with 4 and 6% Mn dopants, respectively.

magnetotransport measurement. **Figure 2** shows the temperature-dependent MR curves of the two samples with an out-of-plane magnetic field. **Figure 2(a)** is the MR curves of the 4% Mn-doped sample, and it shows only positive MR in the whole temperature range. Careful examination could find that the MR curve follows a parabolic shape in the whole temperature range except for a small deviation happening at low magnetic field at 1.9 K. The parabolic dependence exclusively indicates that the orbital MR is dominant in this sample [45], while the small deviation should come from the magnetization-enhanced orbital MR [46]. As the Mn dopants increase to 6%, however, the orbital MR is suppressed, and a negative MR is demonstrated at low temperatures, as shown in **Figure 2(b)**. It implies that the enhanced magnetization in more Mn-doped sample significantly boosts the spin-dependent scattering and thus generating the negative MR [45]. However, as the magnetization becomes weak at high temperatures, the positive MR shows up and the orbital MR is dominant again. Through tuning the Mn-doping concentration in Mn_xGe_{1-x} thin film, the engineering of negative and positive MR is conveniently realized, although it still needs to enlarge the MR value for the potential application in MR sensors.

3.2. MR effect in Mn-rich Mn_xGe_{1-x} coherent nanostructures

To precisely control the MR and seek for a large value in Mn_xGe_{1-x} system, Mn-rich Mn_xGe_{1-x} coherent nanostructures are well designed based on its growth thermal dynamics and kinetics characteristics. As already well documented, Mn atoms preferred to form intermetallic compounds [47, 48] with Ge at high growth temperatures, while they tended to form Mn-rich Mn_xGe_{1-x} coherent nanostructures [27, 44, 49, 50] at low growth temperature. By choosing proper growth conditions, Mn-rich Mn_xGe_{1-x} coherent nanostructures with different morphologies were formed by MBE, and their effect to MR properties are well discussed. Following the same cleaning procedure as described above, Ge substrate was loaded into the MBE chamber for superlattice growth. A high-quality Ge buffer layer was first deposited at 250°C, and then the growth temperature was cooled down to 70°C for the subsequent superlattice growth. Ten periods of Mn_xGe_{1-x} and Ge layers were alternatively deposited on the substrate. By adjusting the nominal thickness of Ge space layer from 6 to 25 nm while keeping the Mn_xGe_{1-x} layer at

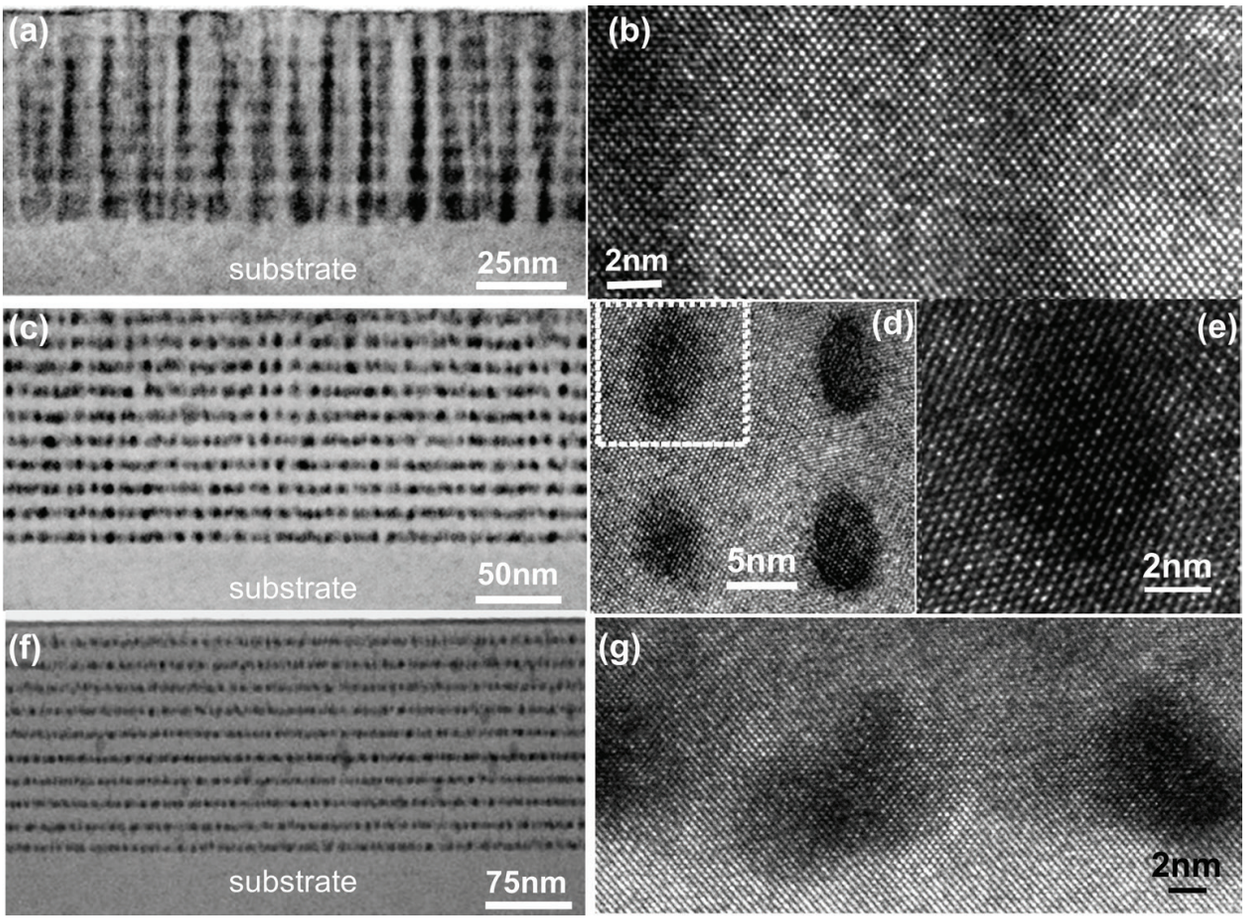

Figure 3. (a) A typical cross-sectional TEM image of the Mn_xGe_{1-x} nanocolumns. (b) Its HRTEM image, showing the coherent Mn_xGe_{1-x} nanocolumns. (c) A typical TEM image of the Mn_xGe_{1-x} nanodots. (d) Its HRTEM image, showing well vertically aligned Mn_xGe_{1-x} nanodots. (e) The zoom-in HRTEM image, showing its diamond lattice structure. (f) A typical TEM image of the nanowell structure. (g) HRTEM image of a single-layer nanowell consisting of coherent MnGe nanodots.

about 4 nm, Mn_xGe_{1-x} nanocolumns, nanodots, and nanowells were obtained, respectively. **Figure 3(a)** shows a typical cross-sectional TEM image of the Mn_xGe_{1-x} nanocolumns with a nominal Ge space layer of 6 nm, in which well-aligned nanocolumns with dark contrast can be clearly observed. To reveal the detailed lattice structure, HRTEM experiments were carried out, and the result is shown in **Figure 3(b)**. Careful examination of the HRTEM image verifies that the Mn_xGe_{1-x} nanocolumns have the same diamond lattice structure as the Ge matrix, showing a coherent growth. The formation of nanocolumns rather than layer structure indicates that Mn atoms not only agglomerate laterally but also migrate vertically into the adjacent Ge space layers [51]. After increasing the Ge space layer thickness to 11 nm, the superlattice evolves from a nanocolumn structure to a nanodot structure. From the cross-sectional TEM image shown in **Figure 3(c)**, 10 periods of nanodots with Ge space layers are clearly observed, in which the nanodots are well aligned along the vertical direction. The alignment may follow the fact that the buried MnGe nanodots induce an elastic strain in the thin Ge space layer, which provides a preferential nucleation site for the formation of new MnGe nanodots. Through further HRTEM characterizations, these nanodots show relatively uniform size distribution with an elliptical shape (dimension of 5.5 ± 0.5 and 8 ± 0.3 nm in the

horizontal and vertical directions, respectively), as demonstrated in **Figure 3(d)**. The fact that the vertical diameter of the nanodot is much larger than the thickness of the MnGe layer again suggests that Mn atoms migrate vertically into the adjacent Ge space layer. **Figure 3(e)** clearly shows the coherent growth of MnGe nanodot in the Ge matrix. After further increasing the Ge space layer thickness to 25 nm, MnGe nanowells with 10 periods were obtained, and a typical TEM image is shown in **Figure 3(f)**. Noticeably, the nanowells are also composed of dense MnGe nanodots, whereas the nanodots are not aligned in the vertical direction. It may be due to the strain release on the top surface of the thick Ge space layer, and hence there are no energy-preferable positions for subsequent nucleation of the MnGe nanodots [52]. Similar to the previous two cases, the MnGe nanodots inside the nanowells are also coherent with the surrounding Ge matrix with a diameter range of 4–10 nm, as shown in **Figure 3(g)**.

The magnetic properties of the formed nanostructures are disclosed by SQUID. Due to the similarity, we took the case of the Mn_xGe_{1-x} nanocolumn as an example, and the result is shown in **Figure 4**. **Figure 4(a)** shows the temperature-dependent M-H curves, which clearly demonstrate the ferromagnetism from 10 to 175 K and the paramagnetism at 300 K. At 10 K, the film exhibits a saturation magnetic moment of 104 kAm^{-1} that is estimated to be 0.24 μ_B per Mn atom. This gives a fraction of 8% of Mn activated in Mn_xGe_{1-x} when considering the value of 3 μ_B in each fully active Mn atom [53]. To further understand its magnetic property, the ZFC and FC curves were performed with a magnetic field of 200 Oe in SQUID, and a typical result is shown in **Figure 4(b)**. The differences between them give an insight into the anisotropic barrier distribution, blocking temperature, and Curie temperature [54]. Two blocking temperatures could be well resolved with one at 25 K and the other at 250 K. As discussed above, the two blocking temperatures indicate the coexistence of Mn-rich Mn_xGe_{1-x} nanostructures and Mn_5Ge_3 nanoparticles in the film. The former has been well recognized in **Figure 3**, whereas the latter could be occasionally observed by comprehensive TEM characterization. Such fact proves that the ZFC and FC measurement in SQUID is more sensitive to detect magnetic particles than TEM [44, 54]. The Curie temperature of the nanocolumns is around 300 K proven from the almost zero magnetic moment at this temperature, which further confirms the existence of Mn_5Ge_3 (T_c ~ 296 K).

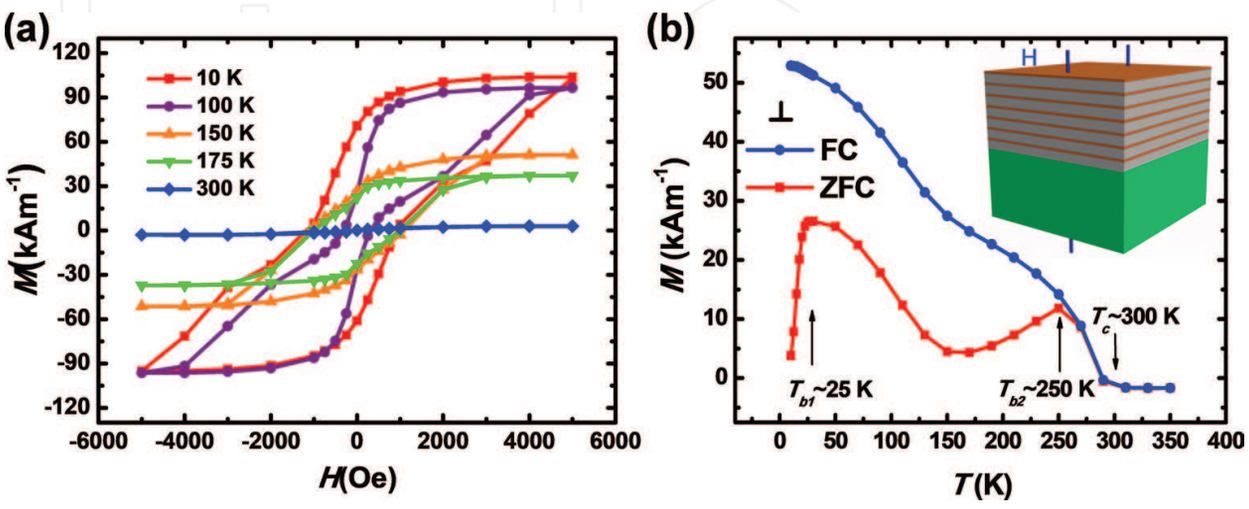

Figure 4. (a) Temperature-dependent hysteresis loops of Mn_xGe_{1-x} nanocolumns with out-of-plane external magnetic field. (b) ZFC and FC curves. Inset is a schematic drawing of the sample setup during the SQUID measurements.

Since the Mn-rich Mn_xGe_{1-x} coherent nanostructures demonstrate different morphologies, it is of great interest to reveal their MR properties and explore the potential application for MR sensors. The samples were fabricated into micrometer-size Hall bar structures, and the measurements were performed in PPMS. The temperature range is from 2 to 300 K with an external magnetic field up to 10 T in an out-of-plane direction. For Mn_xGe_{1-x} nanocolumns, negative MR is observed below 50 K, and a transition to positive MR happens at high temperatures, as shown in **Figure 5(a)**. The origin of the negative MR should come from the spin-dependent scattering mechanism. In the absence of magnetic field, the carrier transport between the nanocolumns with relatively random spin alignment is believed to result in a strong spin-dependent scattering and thus in a high resistance. The high magnetic field would align the spin of the nanocolumns preferentially in one direction. The reduction of spin scattering leads to a low resistance, hence generating a negative MR. The positive MR at high temperatures follows a parabolic shape, which indicates that an orbital MR effect is dominant.

However, the negative MR disappears in Mn_xGe_{1-x} nanowells and nanodot structures, respectively, shown in **Figure 5(b)** and **(c)**, and instead only positive MR presents in the entire temperature range. Careful examination can find that the positive MR in both of the samples does not follow a perfectly parabolic shape and shows very large values at low temperatures. Especially, the MR value in Mn_xGe_{1-x} nanodot structure is as high as 1000% at 2 K, which is hard to be simply explained by orbital MR. Instead, the geometric-enhanced MR due to the existence of conductive Mn_xGe_{1-x} dots is likely to respond to the large MR [24, 43]. To elucidate the underlying physics of the geometric effect, we consider the current density and the total electric field in semiconductors, which can be described by $\mathbf{J} = \boldsymbol{\sigma}(H)\mathbf{E}$, where the $\boldsymbol{\sigma}(H)$ is described as follows:

$$\sigma(H) = \begin{pmatrix} \frac{\sigma}{1+\beta^2} & \frac{\sigma\beta^2}{1+\beta^2} & 0 \\ -\frac{\sigma\beta^2}{1+\beta^2} & \frac{\sigma}{1+\beta^2} & 0 \\ 0 & 0 & \sigma \end{pmatrix} \tag{5}$$

Here, $\beta = \mu H$. In the absence of magnetic field, the tensor $\boldsymbol{\sigma}(H)$ is diagonal, and the current density can be simply described by $\mathbf{J} = \sigma\mathbf{E}$. In this scenario, the current flowing is parallel to the electric field and concentrated into the conductive Mn_xGe_{1-x} nanodots in the Mn_xGe_{1-x} nanowell or nanodot structures, acted as a "short circuit." However, at a high magnetic field, the off-diagonal term of $\boldsymbol{\sigma}(H)$ indicates that the current is deflected from conductive Mn_xGe_{1-x} nanodots to the Mn-dilute Ge matrix with low conductivity, resembling an "open circuit." The transition from the "short circuit" at zero fields to the "open circuit" at high fields produces an increase in resistance. The increased amplitude is significantly dependent on the resistance ratio of Mn_xGe_{1-x} nanodots to the Mn-dilute Ge matrix, and the deflection angle is defined by magnetic field and carrier mobility [24]. Through this mechanism, it is also very simple to explain why the Mn_xGe_{1-x} nanodot structure shows much larger MR compared to Mn_xGe_{1-x} nanowell structure. Compared to Mn_xGe_{1-x} nanodot structure, the disordered conductive nanodots in Mn_xGe_{1-x} nanowell structure make it hard to bypass the conductive nanodots even after deflection around one dot, thus generating lower MR ratio.

http://dx.doi.org/10.5772/intechopen.70206

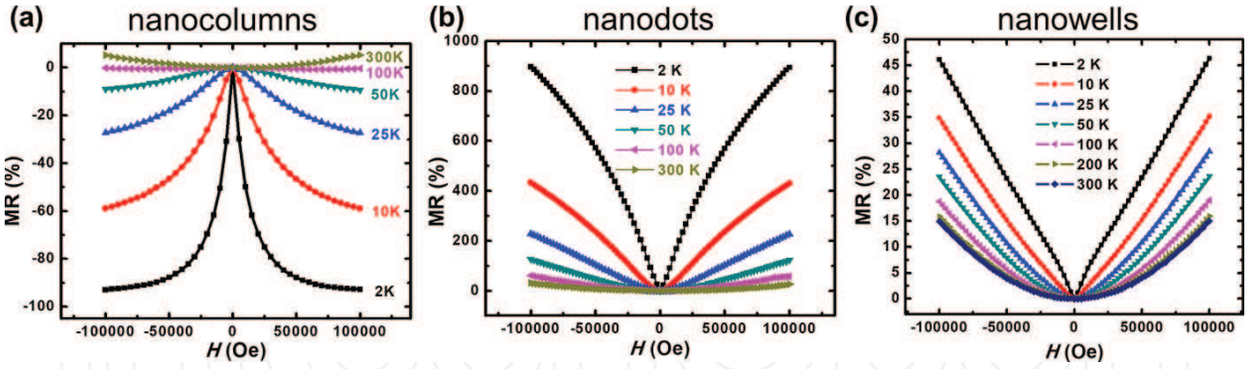

Figure 5. (a)–(c) Temperature-dependent MR curves of the Mn_xGe_{1-x} nanocolumns, nanodots, and nanowells, respectively. The Mn_xGe_{1-x} nanocolumns show negative MR below 50 K, while a positive value dominates at high temperature. For Mn_xGe_{1-x} nanodots and nanowells, however, only positive MR is observed in the whole temperature range from 2 to 300 K.

The above results clearly demonstrate that the negative-to-positive MR and even large MR can be well engineered through well designing the Mn-rich Mn_xGe_{1-x} coherent nanostructures. Therefore, it points out a new direction to easily engineer Mn_xGe_{1-x} nanostructures through strain approach, which may provide a great advantage in designing MR sensors for more functionality.

3.3. Geometric-enhanced and electric-field controlled MR in Mn_xGe_{1-x} nanomesh

The strain engineering of Mn_xGe_{1-x} nanostructures provides a potential approach for satisfying the demand of MR sensors with multifunctionality; however, the self-assembly formation of Mn_xGe_{1-x} nanodots increases the difficulty in accurate control of MR. Therefore, we pay our attention to the pattern-assistant growth of Mn_xGe_{1-x} nanostructures and disclose their MR property. In this section, Mn_xGe_{1-x} nanomesh is demonstrated, which could simultaneously provide the nanostructure benefit [55] and large-scale uniform fabrication [28]. The growth of Mn_xGe_{1-x} nanomesh is also proceeded in the MBE chamber. Before that, great effort has been devoted to fabricate the pattern structure. A 100-nm-thick SiO_2 thin film was firstly deposited on a Ge (111) wafer by PECVD, followed by the formation of a large-scale and close-packed hexagonal single layer of nanospheres on the SiO_2 substrate, as shown in **Figure 6(a)**. By adjusting O_2-plasma etching time, the nanospheres were successfully shrunk to 160 nm with a 60 nm gap between them as shown in **Figure 6(b)**. Using the nanosphere as the mask, the pattern was transferred to the bottom SiO_2 layer by a two-step etching. Dry etching was firstly employed to etch SiO_2 layer till a 10 nm SiO_2 left. Then, wet etching was hired to remove the left SiO_2 layer. After dissolving the nanospheres, periodic SiO_2 nanopillars were obtained on the substrate, and a typical scanning electron microscopy (SEM) image is shown in **Figure 6(c)**. After carefully cleaning, the substrate was loaded into the MBE chamber for the Mn_xGe_{1-x} growth. After degassing at 600°C for 30 min, the patterned substrate was in situ cooled down to 160°C for the Mn_xGe_{1-x} nanomesh growth with a Ge growth rate of 0.2 Å/s and a controlled Mn flux as the dopant source.

The SiO_2 mask was subsequently removed after MBE growth by selective etching, and only Mn_xGe_{1-x} nanomesh was remained. A typical morphology of the sample was captured by SEM

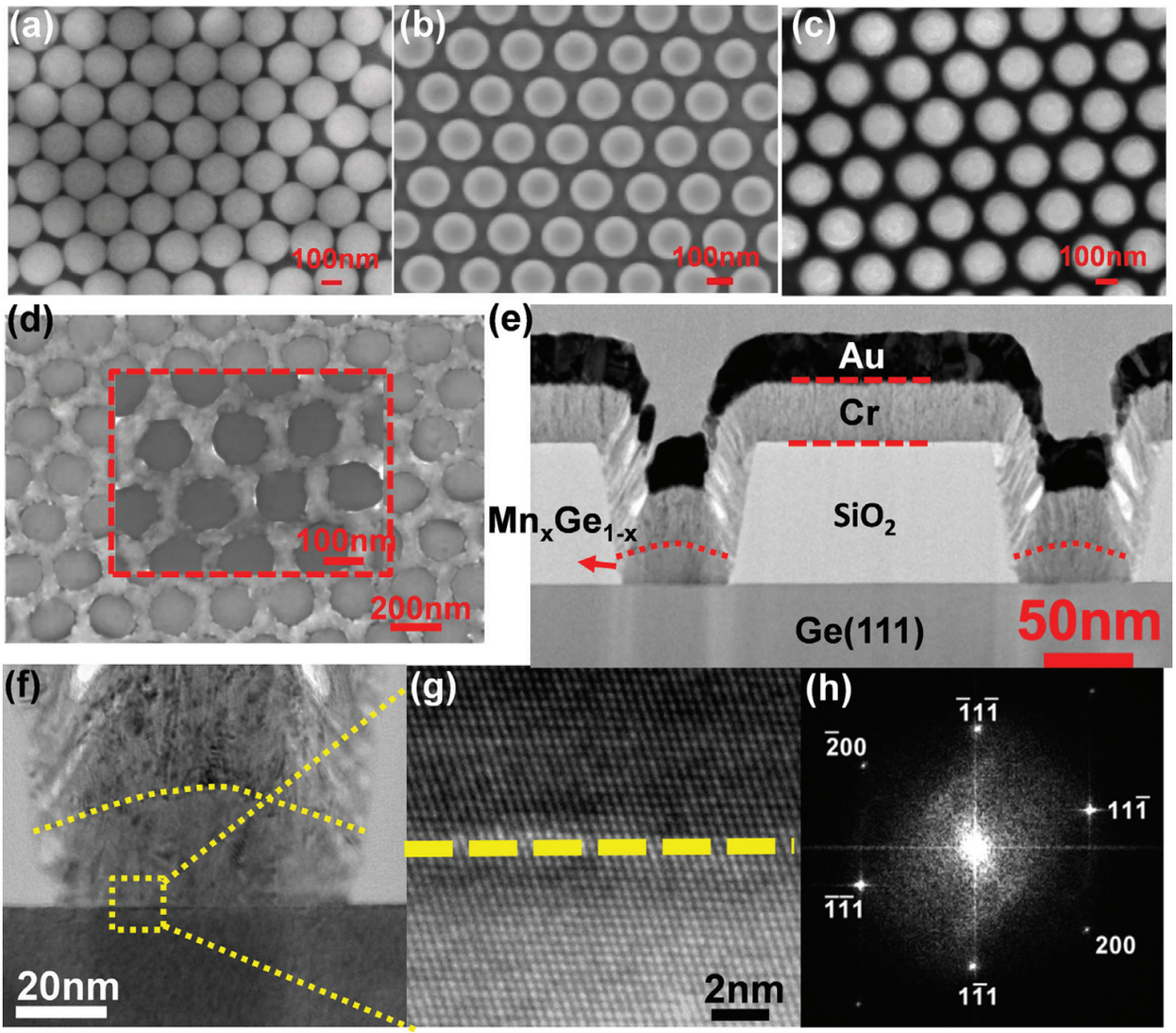

Figure 6. (a) Self-assembly growth of close-packed single layer of nanospheres on the Ge substrate. (b) O_2-plasma etching of the nanospheres to reach the desired size. (c) SiO_2 nanopillars formed by dry etching, masked by the nanospheres. (d) Typical SEM image of the Mn_xGe_{1-x} nanomesh, with a nanomesh width of 60 nm and a nanohole diameter of 160 nm. The inset is the magnified SEM image. (e) Cross-sectional TEM image in a low resolution, showing the Mn_xGe_{1-x} nanomeshes defined well by SiO_2 mask. (f) Magnified cross-sectional TEM image of the Mn_xGe_{1-x} nanomesh. (g) HRTEM image of the interface between the nanomesh and substrate, clearly showing a perfect coherent growth. (h) Its Fourier transform image.

as shown in **Figure 6(d)**. A periodic nanomesh structure exhibits a nanomesh width of 60 nm and a hole diameter of 160 nm; a magnified SEM image is also shown in the inset. To further characterize the microstructure of the formed nanomesh, cross-sectional TEM was employed, and the results are shown in **Figure 6(e)–(h)**. The focused ion beam was employed to cut the sample along the diameter of the hole. Before that, a Cr/Au layer was deposited to protect the sample from damage of the ion beam. **Figure 6(e)** is a low-resolution cross-sectional TEM image of the Mn_xGe_{1-x} nanomesh, which clearly shows that the nanomesh is grown on the Ge substrate as defined by the SiO_2 pattern. The zoom-in image shows that the Mn_xGe_{1-x} nanomesh has a height of 25 nm and a width of 60 nm, consistent with the SEM result. HRTEM

image clearly demonstrates the coherent growth of the Mn_xGe_{1-x} nanomesh on Ge substrate, as shown in **Figure 6(f)**. It does not reveal any observable precipitate. The Fourier transform image as shown in **Figure 6(h)** gives only one set of periodic patterns, indicating a perfect epitaxial growth. This image can be indexed to the [011] zone axis of the Ge diamond lattice, and the epitaxial growth direction is along [111].

SQUID measurement was performed in the following to well understand the magnetic property of the Mn_xGe_{1-x} nanomesh. **Figure 7(a)** shows the temperature-dependent hysteresis loops of the sample, when an external field is applied parallel to the sample surface. The S-shaped hysteresis loops indicate the ferromagnetism above 350 K. **Figure 7(b)** is the magnified hysteresis loop obtained at 10 K, clearly showing a small coercivity of 100 Oe with a saturation magnetization of 0.87 μ_B per Mn. At 350 K, the magnified hysteresis loop demonstrates that the coercivity still remains a value of 40 Oe, as shown in **Figure 7(c)**. Furthermore, Arrott plots [55] were also used to evaluate the T_c, as shown in **Figure 7(d)**. We observe that even at 350 K, the intercept, namely, reciprocal of the susceptibility, does not vanish, indicating that the T_c has not been reached yet. The extrapolated dashed line indicates that the T_c is beyond 350 K, which agrees well with the hysteresis loops. **Figure 7(e)** shows the temperature-dependent M_s ranging from 10 to 400 K, and it clearly shows a weak temperature dependence and a large magnetization remaining at 400 K. All of the data support that the T_c is over 400 K. The temperature-dependent coercivity is shown in **Figure 7(f)**, demonstrating a coercivity decrease from 100 to 35 Oe in the temperature range from 10 to 400 K. The small coercivity indicates the soft ferromagnetism of our sample, which may come from the Mn-dilute nature.

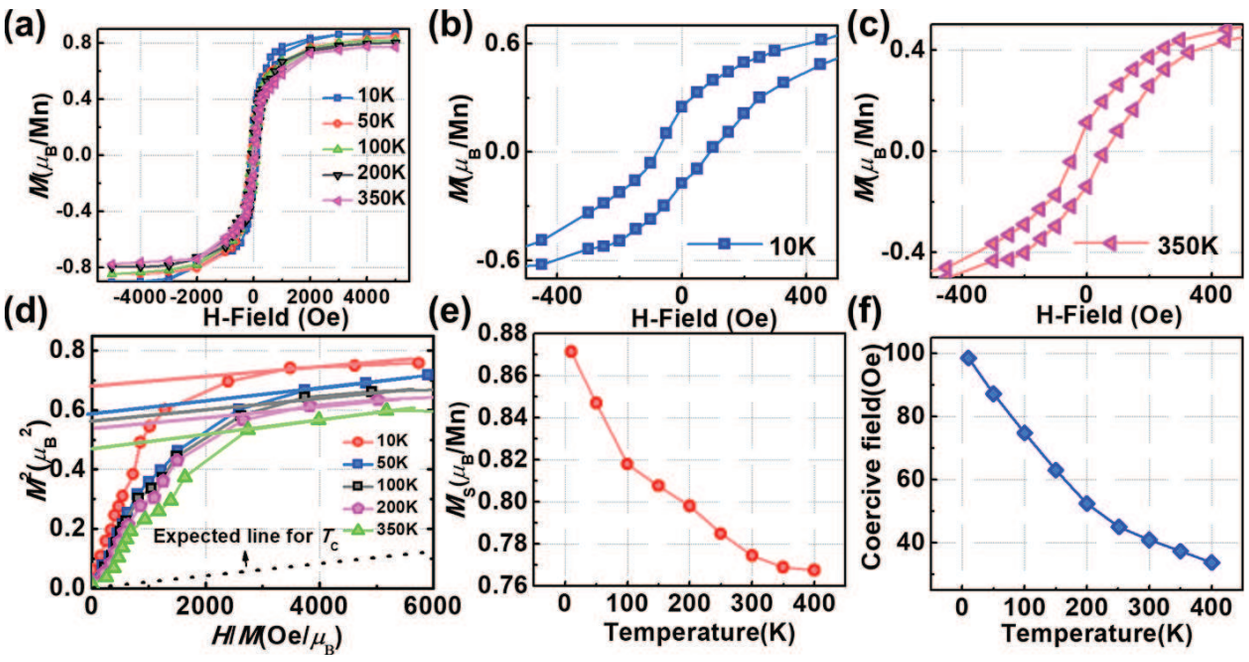

Figure 7. (a) Magnetic hysteresis loops of the Mn_xGe_{1-x} nanomeshes measured at different temperatures from 10 to 350 K. (b)–(c) The magnified hysteresis loop obtained at 10 and 350 K, respectively. (d) Arrott's plots showing that the T_c is above 350 K. (e)–(f) The temperature-dependent saturation moment and coercivity, respectively.

In this unique nanostructure, it is of great interest to investigate its MR property. The sample is fabricated into a micrometer-size Hall bar structure, and the measurement is performed in PPMS, as shown in **Figure 8**. **Figure 8(a)** shows the temperature-dependent resistivity of the Mn_xGe_{1-x} nanomesh under the magnetic field of 0 T (blue square) and 4 T (red circle), respectively, demonstrating a huge difference. A clear metal-to-insulator transition without applying magnetic field (0 T) can be observed with a low-temperature ($T < 30$ K) activation region and a high-temperature ($T > 30$ K) saturation region. Form the Arrhenius relation [56], the activation energy of the nanomesh is estimated to be about 11 meV, which is lower than the substitutional Mn acceptor energy level (160 meV). The underlying mechanism comes from the high-doping level and the presence of exchange interaction, inducing the boarding and possible splitting of the impurity band. Above 30 K, the R-T curve could be well fitted by a power-law relation (T^{α}) with $\alpha \approx 1.6$, close to the value 1.5 predicted for hole scattering by phonons in Ge. The fitting was plotted in red over the blue data in the R-T curve. An intriguing phenomenon is the observation of a giant positive MR in the nanomesh with an out-of-plane magnetic field, as shown in **Figure 8(b)–(d)**. At a magnetic field of 4 T,

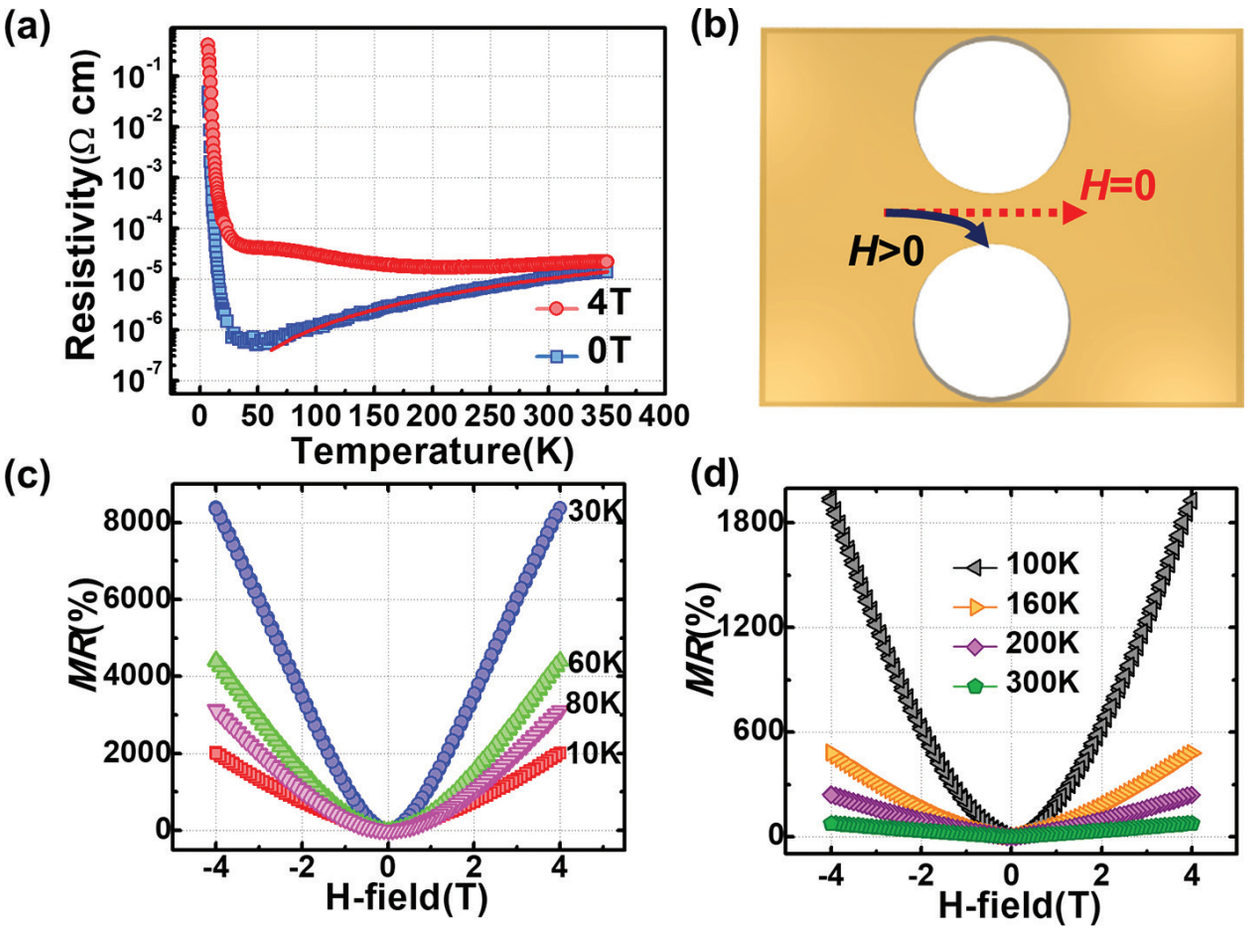

Figure 8. (a) Temperature-dependent resistivity of the Mn_xGe_{1-x} nanomeshes measured without an applied magnetic field (square symbol) and with a magnetic field of 4 T (circle symbol), clearly showing a metal-to-insulator transition. The solid line is the fitting curve. (b) The schematic illustration of scattering mechanism. (c)–(d) Temperature-dependent MR measured at low-temperature and high-temperature regions, respectively.

the MR as high as 2000% at 10 K with the maximum of 8000% at 30 K is observed and still remains 75% at 300 K. Analogously, the giant MR could not be simply attributed to the orbital MR effect, which only contributes a small value. Instead, the geometric-enhanced MR is very plausible to explain the result. To understand this phenomenon, the nanomesh structure could be considered as a highly conductive percolation network with periodic nanoholes. Without applying the magnetic field, the current flows through the Mn_xGe_{1-x} nanomesh with the current directions parallel to the local electric field. As the magnetic field is applied, the current is deflected due to the Lorentz force; the current and local electric fields are no longer collinear. The angle between them is determined by the Hall angle $\theta = \arctan(\mu_H H)$, where the μ_H is the Hall mobility. For a sufficiently high magnetic field, the current is obviously deflected from the highly conductive nanomesh to the insulated nanoholes, resulting in a high resistance. The transition from the extremely low resistance at zero magnetic field to the extremely high resistance at a large magnetic field gives rise to the giant MR, as illustrated in **Figure 8(b)**. Thus, it may be concluded that the lower the initial resistance of the nanomesh is, the larger the MR became at a given magnetic field. It can be verified from the deviation of the R-T curves of 4 T and 0 T, as already shown in **Figure 8(a)**. The largest deviation happens at the lowest resistivity (at 30 K and 0 T), which agrees well with our proposed model.

The Mn_xGe_{1-x} nanomesh is a type of diluted magnetic semiconductor [53, 57] that could provide the ability of electric-field control of ferromagnetism. Therefore, the electric-field controlled MR could be possibly realized to develop new MR sensors with more functionalities. To demonstrate the spin-related MR effect, it is in need of weakening the geometric-enhanced MR effect. One effective approach is to increase the initial resistance of the nanomesh while reducing the carrier mobility. To this end, more Mn-doped Mn_xGe_{1-x} nanomesh was grown, and the transport property is shown in **Figure 9**. **Figure 9(a)** shows the R-T curve of the nanomesh, in which a metal-to-insulator transition is observed; however, the resistivity was found to be more than one order of magnitude larger than the above sample. The increased resistivity may come from the increased scattering center [58]. **Figure 9(b)** and **(c)** shows the temperature-dependent MR curves of the sample. Intriguingly, the geometric-enhanced MR becomes less pronounced, which may be due to the dramatically increased resistivity and the decreased Hall angle from the lower mobility. Instead, a negative MR for temperature below 40 K and a positive MR above 160 K are observed. In the intermediate temperature region (40–160 K), the MR contains two contributions: a positive MR appears at a low magnetic field and a negative slope at high field. Such negative-to-positive MR transition could be attributed to two competitive effects: the spin-dependent scattering by magnetic polarons gave rise to a negative MR [59, 60], and their spatial fluctuations led to the positive MR [59, 60]. As a magnetic field is applied, the carrier mobility increases due to the suppression of the spin-dependent scattering by the magnetic polarons, giving rise to the negative MR, which is proportional to the susceptibility ($\chi(H)$) of the sample. However, the spin-dependent scattering effect by the magnetic polarons decreases with increasing temperature, which makes the positive MR from the spatial fluctuations of magnetic polarons gradually to show up. Due to the strong *p-d* exchange coupling in Mn_xGe_{1-x}, the magnetic polarons will cause a strongly localized valence band splitting into two spin subbands $\varepsilon = \pm 1/2SJM(r)$ [61], where J is the

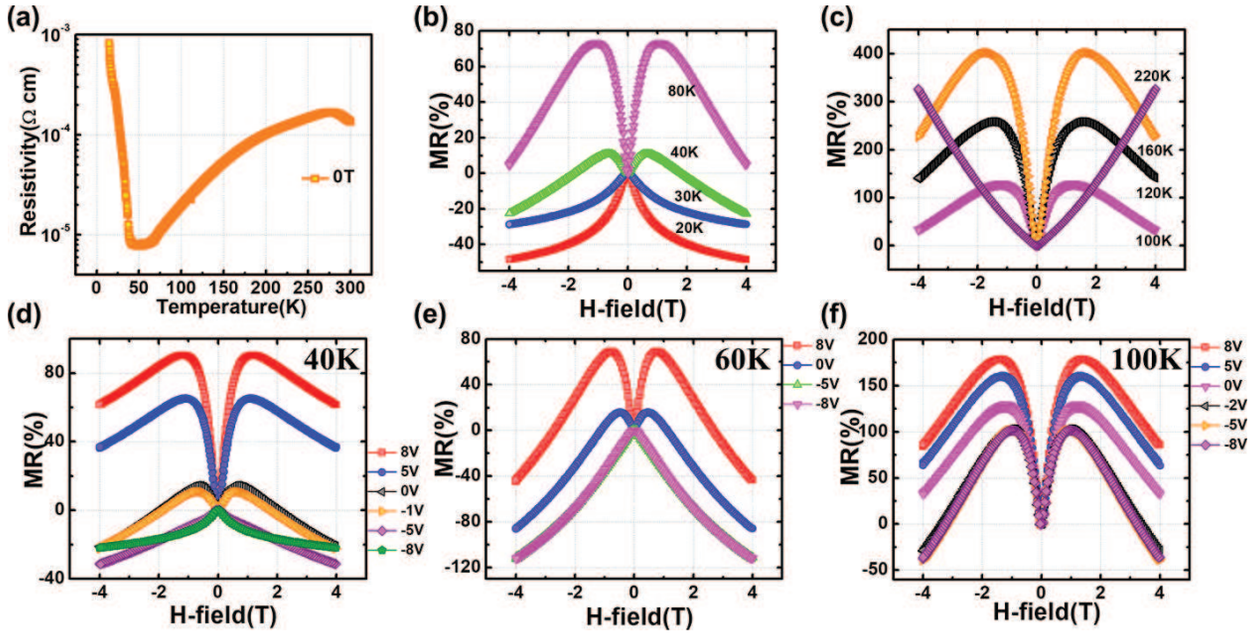

Figure 9. (a) R-T curve of the Mn_xGe_{1-x} nanomeshes with more Mn dopants. (b)–(c) Temperature-dependent MR measured at low-temperature (<80 K) and high-temperature (>100 K) regions, respectively, showing a MR transition from a negative to positive value. (d) Electric-field controlled MR at 40 K, clearly showing a transition from negative to positive when the gate was biased from negative to positive. (e)–(f) Electric-field controlled MR transition at 60 and 100 K, respectively.

exchange coupling energy, S is the spin of electron, and M(r) is the local magnetic moment of the magnetic polaron. This could form a complicated landscape for the valence band with hills and valleys, serving as hole traps. With increasing magnetic field, the hole traps become deeper, the number of itinerant holes decreases, and thus the MR increases. This positive MR is proportional to the square of the magnetization ($M^2(H)$) [59], which can be reflected from the steep slope of the positive MR. As the temperature further increases, the contribution from the spin-dependent scattering becomes weaker, and finally only positive MR dominates the transport.

Furthermore, electric-field control of MR was measured under different gate biases. For that, a 25-nm-thick Al_2O_3 layer was deposited by atomic layer deposition (ALD) on the nanomesh surface as the gate dielectric, followed by the e-beam evaporation of Cr/Au as the gate metal contact. Due to the unique nanomesh structure, the almost-wrap-around gate can be realized to provide a 3D electric-field control of the conduction channel, thus giving a highly efficient and robust carrier modulation. **Figure 9(d)–(f)** shows the gate bias-dependent MR of the Mn_xGe_{1-x} nanomesh sample measured at 40, 60, and 100 K, respectively. When the gate bias changes from −8 to 8 V, a clear negative-to-positive MR transition is observed at 40 K. As described above, this phenomenon should also stem from the competitive effect between the spin-dependent scattering-induced negative MR and the spatial fluctuation-induced positive MR. As already reported [53], the hole-mediated ferromagnetism in Mn-doped Ge enables the electric-field control of magnetic phase transition from a strong ferromagnetism to a soft ferromagnetism, when changing the gate bias from negative to positive. Therefore, as a negative

http://dx.doi.org/10.5772/intechopen.70206

gate bias is applied on our sample, the enhanced ferromagnetism with larger susceptibility ($\chi(H)$) in the Mn_xGe_{1-x} nanomesh could provide a strong spin-dependent scattering, consequently giving rise to a negative MR. When the gate bias is swept to positive value, the weakened ferromagnetism gives rise to a weaker spin-dependent scattering. From another point of view, as the gate bias goes to the positive range, the decreased density of magnetic polarons due to reduced carrier density probably transforms the system from an overlap-together state to a disconnecting state, which thus increases the polaron fluctuation, and hence the positive MR dominates. In addition, gate-dependent MR curves at 60 K and 100 K are shown in **Figure 9(e)** and **(f)**, respectively. At 60 K, the MR transition from the negative to positive value can still be clearly observed when tuning the gate bias. However, the control effect is not as strong as that of 40 K in the negative bias range. This effect can be explained by the fact that even at 0 V, the hole density at 60 K is already high enough to align the magnetic moments of most Mn ions along one direction. Further increasing the negative bias does not significantly enhance the ferromagnetism. At 100 K, it shows a similar effect, i.e., an even weaker control effect in the negative bias range. This extraordinary property may offer a great advantage for designing new MR sensors with voltage-controlled, low-power, high-sensitivity, and nonvolatile functionalities.

4. The potential application of Mn_xGe_{1-x} in MR sensors

The development and utilization of MR sensors have tremendously impacted human beings' life, which refers to a broad range of aspects, including magnetic HDD [4, 23], electric compass [3], biomedical sensors [8, 9], car traffic monitoring [7], and antitheft system [5], among others. The future development in MR sensors should rely on these two perspectives: applications and physics. The discovery of new physics will lead to a new sensor technology toward much smaller size, lower power consumption, lower cost, and higher performance, thus broadening the applications. In turn, the economic benefit from the application will promote further developing high-performance sensors with new physics. In light of that, Mn_xGe_{1-x}-based MR sensors with high compatibility with silicon technology should have a high potential to satisfy this demand. Here, we will give a discussion for its potential application in different functionalized MR sensors.

4.1. High-density information storage

The density of information storage in HDD has significantly increased in the past two decades, which promotes the coming of cloud computing age. The advent of MR read head technology transitioning from the AMR [19] read head to the GMR [34] and TMR [37] read head is the major drive in remarkably increasing storage density of HDD. The GMR and TMR sensors in read head usually comprise two magnetic metal layers separated by a thin nonmagnetic space layer. The basic operation of the magnetoresistance head is to convert the magnetic field that exists above the data bits recorded on the disk to a change in resistance that can be read out. Therefore, the MR sensitivity is extremely important and should be high enough to

distinguish two states (0 and 1); meanwhile, the material for MR sensor could be easily scaled down and integrated with other electric components. Compared to the metal component in current MR sensor, Mn_xGe_{1-x} could have high compatibility with the mature Si technology [54] and hence significantly reduces the manufacturing cost. By utilizing the well-designed giant MR in Mn_xGe_{1-x} system, it will be of much interest to develop Mn_xGe_{1-x}-based MR sensor for high-density magnetic record technology.

4.2. Biomedical sensor

The medical industry has been always striving for noninvasive methods for diagnosing human illness. Due to the electric nature of brain and neuron activity, magnetic sensing is an effective way to detect the brain illness. Meanwhile, it can also be used for unraveling the mystery of the brain how to functionalize, which is of great help for building future brain computer [62] with extremely low power consumption and high performance. Besides, other parts in the body without electric activity can also be detected by magnetic sensor. One effective way is to decorate the cell with nonharmful magnetic particles as the markers. For instance, Wang et al. reported a CMOS magnetic sensor to monitor the pulsatile movements of cardiac progenitor cells tagged with magnetic particles [8]. In addition, magnet tracker can also be used to determine the position of the medical tool inside the body to observe biomechanical motions [3]. In fact, the magnetic signal in biological system normally is very small and usually needs big and heavy equipment for detecting. Therefore, highly sensitive MR sensor is necessary toward miniaturizing the equipment. Mn_xGe_{1-x} appears to be an ideal candidate for fabricating biomedical MR sensor with high sensitivity, high compatibility with CMOS technology, and no poison to human body.

5. Conclusion

MR sensors have dramatically changed the life of human beings in a wide range of applications, including automotive sensor, traffic monitor, mobile phone, HDD, and biomedical sensors, among others. The MR sensors are being developed toward much lower cost, lower power consumption, higher compatibility with CMOS technology, and higher sensitivity. Addressing such demand calls for new material candidate with new physics, improved sensitivity, and easy manufacturing. In this context, we give a review in the recent progress in Mn_xGe_{1-x} system, including material growth and magnetic and magnetotransport properties. The Mn_xGe_{1-x} evolved from thin-film superlattice to patterned nanostructures, and their MR behavior could be well engineered and transformed between the negative and positive. Furthermore, geometric-enhanced giant MR as high as 8000% at 30 K at 4 T is demonstrated. More intriguingly, the electric-field controlled MR emerges, which not only demonstrates great physical meaning but also significantly enhances the functionality of MR sensors with more tuning dimensions. The Mn_xGe_{1-x} system with the advantages of well-controlled MR, and high compatibility with Si technology may set a stage for designing a new breed of MR sensors applicable in magnetic read head and biomedical sensor with much higher performance.

Acknowledgements

This work is supported by the National Natural Science Foundation of China under Grant Nos. 11644004 and 61627813 and the International Collaboration Project B16001. We also gratefully acknowledge the FAME Center, one of the six centers of STARnet, a Semiconductor Research Corporation (SRC) program sponsored by MARCO and DARPA.

Author details

Tianxiao Nie[1,2]*, Weisheng Zhao[1] and Kang L. Wang[2]

*Address all correspondence to: nietianxiao@gmail.com

1 Fert Beijing Institute, BDBC, and School of Electronic and Information Engineering, Beihang University, Beijing, China

2 Device Research Laboratory, Department of Electrical Engineering, University of California, Los Angeles, California, USA

References

[1] Clarke J, Koch RH. The impact of high-temperature superconductivity on SQUID magnetometers. Science. 1988;**242**:217-223

[2] Meydan T. Application of amorphous materials to sensors. Journal of Magnetism & Magnetic Materials. 1994;**133**:525-532

[3] Ripka P. Magnetic Sensors and Magnetometers. Vol. 13; 2002

[4] Fullerton EE, Childress JR. Spintronics, magnetoresistive heads, and the emergence of the digital world. Proceedings of the IEEE. 2016;**104**:1787-1795

[5] Lenssen KMH, Adelerhof DJ, Gassen HJ, Kuiper AET, Somers GHJ, Zon JBADV. Robust giant magnetoresistance sensors. Sensors & Actuators A Physical. 2000;**85**:1-8

[6] Lenz JE. A review of magnetic sensors. Proceedings of the IEEE. 1990;**78**:973-989

[7] Ryoo Y-J, Park J-H. Design and development of magnetic position sensor for magnetic guidance system of automated ground vehicle. In: 2012 12th International Conference on Control, Automation and Systems (ICCAS): IEEE; 2012. pp. 988-991

[8] Wang H, Mahdavi A, Tirrell DA, Hajimiri A. A magnetic cell-based sensor. Lab on a Chip. 2012;**12**:4465-4471

[9] Baselt DR, Lee GU, Natesan M, Metzger SW, Sheehan PE, Colton RJ. A biosensor based on magnetoresistance technology. Biosensors & Bioelectronics. 1998;**13**:731-739

[10] Mujika M, Arana S, Castaño E, Tijero M, Vilares R, Ruano-López JM, Cruz A, Sainz L, Berganza J. Magnetoresistive immunosensor for the detection of *Escherichia coli* O157:H7 including a microfluidic network. Biosensors & Bioelectronics. 2009;**24**:1253

[11] Valenzuela R, Vazquez M, Hernando A. A position sensor based on magnetoimpedance. Journal of Applied Physics. 1996;**79**:6549-6551

[12] Huang WS, Lu CC, Jeng JT. A novel 3D CMOS micro-fluxgate magnetic sensor for low magnetic field detection. In: 2010 IEEE Sensors; 2010. Pp. 1791-1794

[13] Reig C, Mukhopadhyay SC, Cardoso S. Giant magnetoresistance (GMR) sensors. Vol. 6; 2013

[14] Heidari H, Bonizzoni E, Gatti U, Maloberti F. A CMOS current-mode magnetic hall sensor with integrated front-end. IEEE Transactions on Circuits and Systems I: Regular Papers. 2015;**62**:1270-1278

[15] Baibich MN, Broto JM, Fert A, Van Dau FN, Petroff F, Etienne P, Creuzet G, Friederich A, Chazelas J. Giant magnetoresistance of (001)Fe/(001)Cr magnetic superlattices. Physical Review Letters. 1988;**61**:2472-2475

[16] Binasch G, Grünberg P, Saurenbach F, Zinn W. Enhanced magnetoresistance in layered magnetic structures with antiferromagnetic interlayer exchange. Physical Review B. 1989;**39**:4828-4830

[17] Ferreira R, Wisniowski P, Freitas PP, Langer J, Ocker B, Maass W. Tuning of MgO barrier magnetic tunnel junction bias current for picotesla magnetic field detection. Journal of Applied Physics. 2006;**99**:08K706-708K709

[18] Ikeda S, Hayakawa J, Ashizawa Y, Lee YM, Miura K, Hasegawa H, Tsunoda M, Matsukura F, Ohno H. Tunnel magnetoresistance of 604% at 300K by suppression of Ta diffusion in CoFeB/MgO/CoFeB pseudo-spin-valves annealed at high temperature. Applied Physics Letters. 2008;**93**:082508-082510

[19] Tsang C, Chen MM, Yogi T, Ju K. Gigabit density recording using dual-element MR/inductive heads on thin-film disks. In: Magnetics Conference, 1990. Digests of Intermag '90. International, p CA; 1990

[20] Heim DE, Fontana RE, Jr, Tsang C, Speriosu VS. Design and operation of spin valve sensors. IEEE Transactions on Magnetics. 1994;**30**:316-321

[21] Maat S, Marley AC. Physics and Design of Hard Disk Drive Magnetic Recording Read Heads. Netherlands: Springer; 2016

[22] Charap SH, Lu PL, He Y. Thermal stability of recorded information at high densities. IEEE Transactions on Magnetics. 1997;**33**:978-983

[23] Moser A, Takano K, Margulies DT, Albrecht M, Sonobe Y, Ikeda Y, Sun S, Fullerton EE. Magnetic recording: Advancing into the future. Journal of Physics D: Applied Physics. 2002;**35**:R157-R167

[24] Solin SA, Thio T, Hines DR, Heremans JJ. Enhanced room-temperature geometric magnetoresistance in inhomogeneous narrow-gap semiconductors. Science. 2000;**289**:1530-1532

[25] Thio T, Solin SA. Giant magnetoresistance enhancement in inhomogeneous semiconductors. Applied Physics Letters. 1998;**72**:3497-3499

[26] Nie T, Tang J, Wang KL. Quest for high-Curie temperature Mn_xGe_{1-x} diluted magnetic semiconductors for room-temperature spintronics applications. Journal of Crystal Growth. 2015;**425**:279-282

[27] Faxian X, Yong W, Kin W, Yi Z, Xufeng K, Jin Z, Wang KL. MnGe magnetic nanocolumns and nanowells. Nanotechnology. 2010;**21**:255602-255606

[28] Nie T, Tang J, Kou X, Gen Y, Lee S, Zhu X, He Q, Chang L-T, Murata K, Fan Y, Wang KL. Enhancing electric-field control of ferromagnetism through nanoscale engineering of high-Tc Mn_xGe_{1-x} nanomesh. Nature Communications. 2016;**7**:12866

[29] Fert A, Campbell IA. Electrical resistivity of ferromagnetic nickel and iron based alloys. Journal of Physics F Metal Physics. 2001;**6**:849-871

[30] Berkowitz AE, Mitchell JR, Carey MJ, Young AP, Zhang S, Spada FE, Parker FT, Hutten A, Thomas G. Giant magnetoresistance in heterogeneous Cu-Co alloys. Physical Review Letters. 1992;**68**:3745-3748

[31] Xiao JQ, Jiang JS, Chien CL. Giant magnetoresistance in nonmultilayer magnetic systems. Physical Review Letters. 1992;**68**:3749-3752

[32] Hylton TL. Limitations of magnetoresistive sensors based on the giant magnetoresistive effect in granular magnetic composites. Applied Physics Letters. 1993;**62**:2431-2433

[33] Hylton TL, Coffey KR, Parker MA, Howard JK. Giant magnetoresistance at low fields in discontinuous NiFe-Ag multilayer thin films. Science. 1993;**261**:1021-1024

[34] Hylton TL, Coffey KR, Parker MA, Howard JK. Low field giant magnetoresistance in discontinuous magnetic multilayers. Journal of Applied Physics. 1994;**75**:7058-7060

[35] Moodera JS, Kinder LR, Wong TM, Meservey R. Large magnetoresistance at room temperature in ferromagnetic thin film tunnel junctions. Physical Review Letters. 1995;**74**:3273-3276

[36] Miyazaki T, Tezuka N. Giant magnetic tunneling effect in $Fe/Al_2O_3/Fe$ junction. Journal of Magnetism & Magnetic Materials. 1995;**139**:L231-L234

[37] Parkin SSP, Kaiser C, Panchula A, Rice PM, Hughes B, Samant M, Yang SH. Giant tunnelling magnetoresistance at room temperature with MgO (100) tunnel barriers. Nature Materials. 2004;**3**:862-867

[38] Wang KL, Kou X, Upadhyaya P, Fan Y, Shao Q, Yu G, Amiri PK. Electric-field control of spin-orbit interaction for low-power spintronics. Proceedings of the IEEE. 2016;**104**:1974-2008

[39] Heimbrodt W, Klar PJ, Ye S, Lampalzer M, Michel C, Baranovskii SD, Thomas P, Stolz W. Magnetic interactions in granular paramagnetic–ferromagnetic GaAs: Mn/MnAs hybrids. Journal of Superconductivity and Novel Magnetism. 2005;**18**:315-320

[40] Lin JH, Wu YQ, Tang S, Fan YL, Yang XJ, Jiang ZM, Zou J. Composition and strain measurements of Ge(Si)/Si(001) islands by HRTEM. Journal of Nanoscience and Nanotechnology. 2009;**9**:2753-2757

[41] Dedkov YS, Holder M, Mayer G, Fonin M, Preobrajenski AB. Spin-resolved photoemission of a ferromagnetic MnSGe3(0001) epilayer on Ge(111). Journal of Applied Physics. 2009;**105**:073909-073912

[42] Petit M, Michez L, Dutoit CE, Bertaina S, Dolocan VO, Heresanu V, Stoffel M, Thanh VL. Very low-temperature epitaxial growth of Mn5Ge3 and Mn5Ge3C0.2 films on Ge(111) using molecular beam epitaxy. Thin Solid Films. 2015;**589**:427-432

[43] Jamet M, Barski A, Devillers T, Poydenot V, Dujardin R, Bayle-Guillemaud P, Rothman J, Bellet-Amalric E, Marty A, Cibert J, Mattana R, Tatarenko S. High-Curie-temperature ferromagnetism in self-organized $Ge_{1-x}Mn_x$ nanocolumns. Nature Materials. 2006;**5**:653-659

[44] Devillers T, Jamet M, Barski A, Poydenot V, Bayle-Guillemaud P, Bellet-Amalric E, Cherifi S, Cibert J. Structure and magnetism of self-organized $Ge_{1-x}Mn_x$ nanocolumns on Ge(001). Physical Review B. 2007;**76**:205306-205315

[45] Park YD, Wilson A, Hanbicki AT, Mattson JE, Ambrose T, Spanos G, Jonker BT. Magnetoresistance of Mn:Ge ferromagnetic nanoclusters in a diluted magnetic semiconductor matrix. Applied Physics Letters. 2001;**78**:2739-2741

[46] Nie T, Kou X, Tang J, Fan Y, Lang M, Chang L-T, Chu C-P, He L, Lee S-W, Xiu F. Superlattice of Fe_xGe_{1-x} nanodots and nanolayers for spintronics application. Nanotechnology. 2014;**25**:505702-505708

[47] Wang Y, Zou J, Zhao Z, Han X, Zhou X, Wang KL. Mn behavior in Ge[sub 0.96]Mn[sub 0.04] magnetic thin films grown on Si. Journal of Applied Physics. 2008;**103**:066104-066103

[48] Wang Y, Xiu F, Wang Y, Xu H, Li D, Kou X, Wang KL, Jacob AP, Zou J. Effect of Mn concentration and growth temperature on nanostructures and magnetic properties of $Ge_{1-x}Mn_x$ grown on Si. Journal of Crystal Growth. 2010;**312**:3034-3039

[49] Xiu F, Wang Y, Kou X, Upadhyaya P, Zhou Y, Zou J, Wang KL. Synthesis of High-Curie-Temperature Fe0.02Ge0.98 quantum dots. Journal of The American Chemical Society. 2010;**132**:11425-11427

[50] Xiu F, Wang Y, Kim J, Hong A, Tang J, Jacob AP, Zou J, Wang KL. Electric-field-controlled ferromagnetism in high-Curie-temperature Mn0.05Ge0.95 quantum dots. Nature Materials. 2010;**9**:337-344

[51] Wang Y, Xiu F, Wang Y, Zou J, Beyermann WP, Zhou Y, Wang KL. Coherent magnetic semiconductor nanodot arrays. Nanoscale Research Letters. 2011;**6**:134-141

[52] Chen YW, Pan BY, Nie TX, Chen PX, Lu F, Jiang ZM, Zhong ZY. Enhanced photoluminescence due to lateral ordering of GeSi quantum dots on patterned Si(001) substrates. Nanotechnology. 2010;**21**:175701-175704

[53] Park Y, Hanbicki A, Erwin S, Hellberg C, Sullivan J, Mattson J, Ambrose T, Wilson A, Spanos G, Jonker B. A group-IV ferromagnetic semiconductor: Mn_xGe_{1-x}. Science. 2002;**295**:651-654

[54] Nie T, Kou X, Tang J, Fan Y, Lee S, He Q, Chang L-T, Murata K, Gen Y, Wang KL. Nanoengineering of an Si/MnGe quantum dot superlattice for high Curie-temperature ferromagnetism. Nanoscale. 2017;**9**:3086-3094

[55] Faxian X, Yong W, Jiyoung K, Hong A, Jianshi T, Jacob AP, Jin Z, Wang KL. Electric-field-controlled ferromagnetism in high-Curie-temperature Mn 0.05Ge 0.95 quantum dots. Nature Materials. 2010;**9**:337-344

[56] Chang L-T, Wang C-Y, Tang J, Nie T, Jiang W, Chu C-P, Arafin S, He L, Afsal M, Chen L-J, Wang K L. Electric-field control of ferromagnetism in Mn-doped ZnO nanowires. Nano Letters. 2014;**14**:1823-1829

[57] Ohno H, Chiba D, Matsukura F, Omiya T, Abe E, Dietl T, Ohno Y, Ohtani K. Electric-field control of ferromagnetism. Nature. 2000;**408**:944-946

[58] Iye Y, Oiwa A, Endo A, Katsumoto S, Matsukura F, Shen A, Ohno H, Munekata H. Metal–insulator transition and magnetotransport in III–V compound diluted magnetic semiconductors. Materials Science and Engineering: B. 1999;**63**:88-95

[59] Li AP, Zeng C, van Benthem K, Chisholm MF, Shen J, Nageswara Rao SVS, Dixit SK, Feldman LC, Petukhov AG, Foygel M, Weitering HH. Dopant segregation and giant magnetoresistance in manganese-doped germanium. Physical Review B. 2007;**75**:201201-201204

[60] Li AP, Wendelken JF, Shen J, Feldman LC, Thompson JR, Weitering HH. Magnetism in Mn_xGe_{1-x} semiconductors mediated by impurity band carriers. Physical Review B. 2005;**72**:195205-195213

[61] Haas C. Spin-disorder scattering and magnetoresistance of magnetic semiconductors. Physical Review. 1968;**168**:531-538

[62] Huang Y, Kang W, Zhang X, Zhou Y, Zhao W. Magnetic skyrmion-based synaptic devices. Nanotechnology. 2017;**28**:08LT02-08LT08

IntechOpen